

Multi-kilometre and multi-gigabit-per-second sub-terahertz communications for wireless backhaul applications

Received: 17 June 2021

Accepted: 13 November 2022

Published online: 30 December 2022

 Check for updates

Priyangshu Sen¹, Jose V. Siles², Ngwe Thawdar³ & Josep M. Jornet¹


Sub-terahertz- and terahertz-band—that is, from 100 GHz to 10 THz—communication technologies will be required for next-generation (6G and beyond) wireless communication networks. Considerable progress has been made in terahertz device technology for personal and local area networks, but there are many applications that could benefit from the large capacity of sub-terahertz and terahertz wireless links if longer communication distances were possible. The generation of high-power information-bearing ultrabroadband signals for long-distance communication is though challenging. Here we report a multi-kilometre and multi-gigabit-per-second link operating at 210–240 GHz. We use on-chip power-combining frequency multiplier designs based on Schottky diode technology to achieve a transmit power of 200 mW. A tailored software-defined ultrabroadband digital signal processing back end is also used to generate the modulated signal and process it in the receiver.

The need to provide faster wireless data rates to an ever-increasing number of wirelessly connected devices is driving a search for untapped spectral resources. Under 95 GHz, spectrum auctions for fifth-generation cellular systems at 24–28 GHz (ref. 1) and 37–47 GHz (ref. 2), WiFi networks at 57–64 GHz, fixed and mobile links at 71–76 GHz and 81–86 GHz, and the vehicular radar band at 77 GHz are progressively crowding the spectrum. In March 2019, the US Federal Communications Commission (FCC) approved the first regularization of the electromagnetic spectrum between 95 GHz and 3 THz (ref. 3). Over 20 GHz of non-consecutive bandwidth was allocated for unlicensed services at frequencies between 95 and 275 GHz. Procedures for industry and academia to obtain experimental licences were also streamlined. This has opened the door to innovative communication applications in the terahertz band^{4–6}, which we define here as the spectrum between 100 GHz and 10 THz.

The large bandwidth available at terahertz frequencies could decongest the lower-frequency bands and enable ultrahigh-bandwidth applications for future wireless systems, including massive multicore wireless networks on chip⁷, terabit-per-second wireless personal area

networks, broadband backhaul connectivity for rural Internet access and high-speed intersatellite links⁸. However, this large bandwidth comes at the cost of high propagation loss^{9,10}. The small wavelength of terahertz signals—3 mm at 100 GHz to 30 μm at 10 THz—requires small antennas, which could deliver some of the aforementioned on-chip network applications. However, this results in small antenna effective areas and thus high power-spreading losses. To compensate for this, larger, high-gain directional antennas need to be used. For a fixed antenna footprint, the antenna gain increases with frequency, but must become more directional. Additionally, the photon energy of terahertz signals (from 0.4 to 40.0 meV)—although non-ionizing—triggers vibrational rotational modes in gaseous molecules (especially water vapour), which lead to strong absorption lines across the terahertz band. These are of interest to the remote and atmospheric sensing community, but from the communication perspective, they result in high path loss and narrower transmission bandwidths.

For many years, this high path loss, combined with the lack of compact and efficient signal sources, mixers and detectors, has limited the feasibility of long-range communications in the terahertz band.

¹Department of Electrical and Computer Engineering, Northeastern University, Boston, MA, USA. ²NASA Jet Propulsion Laboratory Submillimeter-Wave Advanced Technology Group, Pasadena, CA, USA. ³Air Force Research Laboratory, Information Directorate, Rome, NY, USA.  e-mail: sen.pr@northeastern.edu; jose.v.siles@jpl.nasa.gov; ngwe.thawdar@us.af.mil; j.jornet@northeastern.edu

Recently, developments in material and device technologies have begun to address these issues¹¹. In the case of the electronics approach, standard silicon complementary metal–oxide–semiconductor technology¹², silicon–germanium bipolar complementary metal–oxide–semiconductor technology¹³, III–V semiconductor high-electron-mobility transistors¹⁴, metamorphic high-electron-mobility transistors¹⁵, heterojunction bipolar transistors¹⁶ and Schottky diode¹⁷ technologies are being pushed to reach the 1 THz mark. In photonics, unitravelling carrier photodiodes¹⁸, photoconductive antennas¹⁹, optical downconversion systems²⁰ and quantum cascade lasers²¹ are being investigated for high-power systems. In parallel to device technology accomplishments, communication strategies tailored to the peculiarities of the terahertz wireless channel are being developed, including time, frequency and phase synchronization strategies for ultrabroadband channels²², robust terahertz channel estimation and equalization techniques²³, as well as innovative waveform designs for distance-dependent absorption-defined transmission windows^{24,25}.

In this Article, we report a multi-gigabit-per-second (beyond 2 Gbps) link operating at 210–230 GHz over a distance of 2.03 km. We use 200 mW terahertz signal sources and low-noise broadband balanced frequency mixers based on Schottky diode technology in combination with custom-designed communication and signal processing techniques implemented on a software-defined ultrabroadband (30 GHz) digital baseband system. The jointly developed hardware, software system and channel environment of the point-to-point link is illustrated in Fig. 1. Our approach illustrates the potential of high-capacity wireless backhaul links, which could be used to carry the aggregated data traffic of multiple users operating in the microwave and millimetre-wave spectrum. Wireless backhaul technology, with its low complexity, can be deployed at a fraction of the cost of wired technologies, facilitating access to the spectrum for traditionally underserved areas. It could, for example, be of use in rural broadband connectivity or in emergency networks following extreme events such as earthquakes.

High-power transceivers

The key hardware components in the system are the Schottky-diode-based frequency multipliers and low-noise ultrabroadband frequency mixers. The devices were designed in-house and fabricated utilizing the flight-qualified NASA JPL air-bridge planar Schottky diode process used for the Herschel-heterodyne instrument for the far-infrared (HIFI) instrument onboard the Herschel Space Observatory²⁶ and the microwave instrument onboard the Rosetta Orbiter (MIRO)²⁷. The complete multiplier and mixer structure is fabricated on a single gallium arsenide (GaAs) monolithic microwave integrated circuit. The process enables a high level of integration, which allows the use of multiple anodes on the same chip. Furthermore, it improves the control of critical matching circuit elements, which is crucial at frequencies above 100 GHz. The enabling technology to achieve over 200 mW of transmitted power at the centre frequency of our experiments (225 GHz) is the NASA JPL-patented multiplier technology based on on-chip power combining^{28,29}. This concept allows combining several multiplier structures in a single chip, increasing the number of diodes on the chip by a factor of four. By a thorough optimization of the diode epitaxy and chip layout for high-power operation, the technology allows the increase of output power per chip by a factor of 10 compared with traditional terahertz-frequency-multiplier sources. Details about the fabrication process is discussed in the Methods section.

The block diagram of the transmitter is illustrated in Fig. 1c. The lack of a frequency mixer at radio frequency (RF) that can support the high output power of the last block in the frequency multiplier chain prevents us from utilizing a traditional heterodyne transmitter configuration with a mixer before the antenna. Instead, two different system configurations are considered. In the first configuration (upconverter 1), the local oscillator (LO) is directly modulated before

being injected in the frequency multiplier chain. In this case, to ensure that the frequency multipliers are always active, a minimum LO signal power is always needed, discouraging the use of on–off keying (OOK) or amplitude modulations. As a result, phase modulations are preferred. However, the phase of the modulated LO signal is affected by the nonlinear response of frequency multipliers, and thus, careful waveform engineering is needed at the LO. In the second configuration (upconverter 2), a harmonic mixer is placed between the two multiplier stages. In this case, only the nonlinear response of the last frequency multiplier needs to be taken into account. However, the mixer introduces non-negligible conversion losses. Also, for simplicity, the power amplifiers and attenuators are omitted from the transceiver figures, which are utilized to maintain power requirements in different stages.

In Fig. 2a, the measured radiated power at RF is shown for the two cases. For upconverter 1, the power is measured by changing the LO power frequency. For upconverter 2, the response is measured by injecting an intermediate frequency (IF) at 10 GHz with –16 dBm and sweeping the LO. The tripler in upconverter 2 was purposely designed for higher power, allowing to compensate for the conversion loss of the mixer. However, the mixing process leads to multiple harmonics, but only one of them contains the modulated signal with minimal distortion (Methods). As a result, the power at this frequency component is approximately 10 dB lower than the total power of upconverter 2 (Fig. 2a). In both cases, having an adequate transmission power opens the door to long-range terahertz communications. Beyond the transmitted power, the frequency selectivity of the transmitter as well as phase distortion introduced by frequency multipliers need to be taken into account when designing the signal processing blocks at the transmitter and receiver, as discussed in the next section.

The block diagram of the receiver with multipliers and mixers is shown in Fig. 1d. In this case, a low-power frequency multiplier chain is utilized to drive the receiver mixer at RF, which is now possible due to the expectedly much lower power of the received signals. The mixer design has been optimized for low conversion loss and low noise temperature over a large frequency band. The mixer topology is based on a Schottky-diode-based balanced mixer traditionally used in Earth and planetary science missions developed at JPL^{30,31} (Fig. 1e). The mixer design consists of a planar monolithic microwave integrated circuit process developed at JPL during the last two decades. The employed mixer consists of two Schottky diodes in a balanced configuration that allows optimizing the IF signal at f_{RF} from f_{LO} and minimizing the power to undesired harmonics or intermodulation products. The mixer diodes and planar circuitry are fabricated together on a GaAs wafer. The LO is coupled to the mixer chip via an LO input probe integrated into the mixer chip and suspended on the LO input waveguide. Similarly, the RF signal is injected into the chip through a second input waveguide. Mixing occurs in the nonlinear Schottky diodes and the resulting IF signal is transferred to the IF output. On-chip low-pass IF filters are used to prevent LO and RF signals to leak to the IF output. Further, additional waveguide-matching sections are used in the block to optimize the chip performance at the desired bandwidth. The anode size and epitaxial structure of the diodes are also carefully designed to maximize performance at the desired frequency. As illustrated in Fig. 2b, the conversion loss is approximately 5 dB between 210 and 240 GHz, and the noise temperature is under 1,000 K between 212 and 232 GHz. This opens the door to broadband wireless links at terahertz frequencies.

The amplitude and phase noise statistics of the receiver are shown in Fig. 2c,d, respectively. The histogram of the measured noise amplitude (for 10 GHz of receiver mixer bandwidth) follows a Gaussian distribution, with approximated mean and variance of 0.01 mV and 1.01 μW , respectively. Therefore, the N_0 value is $1.01 \times 10^{-16} \text{ W Hz}^{-1}$ for our receiver system.

The estimated and measured single-sideband (SSB) phase noise in terms of decibels relative to the carrier per Hertz (dBc Hz^{-1}) are shown in Fig. 2d for both end-to-end systems. The mismatch between the estimated and measured values are due to the additional components

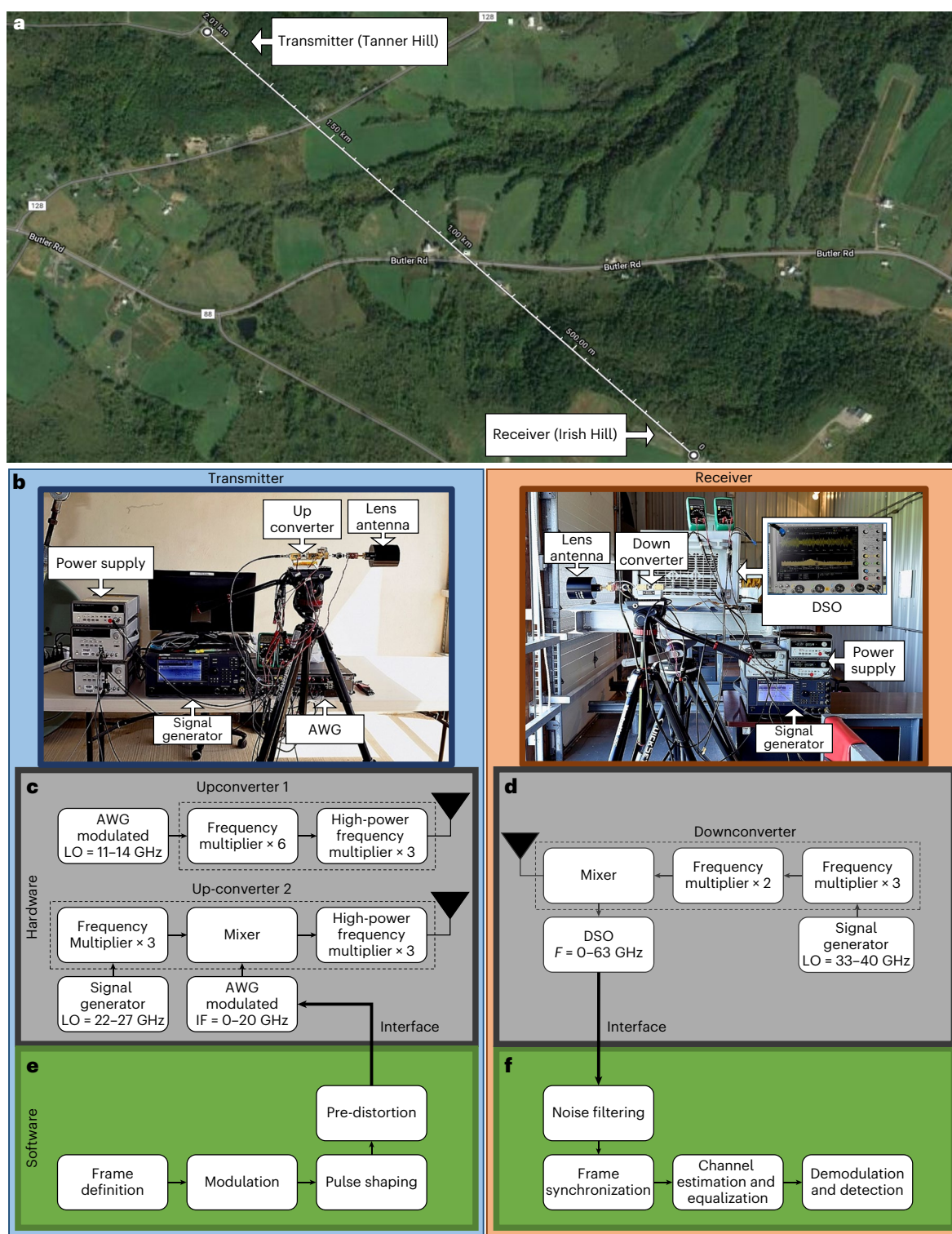


Fig. 1 Experimental setup and system design at 210–240 GHz. **a**, Channel environment of 2 km point-to-point link at the Air Force Research Laboratory research facility. **b**, The developed terahertz communication system. **c,d**, Block diagram for the transmitter (**c**) and receiver (**d**) hardware. **e,f**, Signal processing and communication blocks at the transmitter (**e**) and receiver (**f**).

in the system that also contribute to phase noise, including mixers and amplifiers^{32,33}. The main contributor to phase noise is the reference phase noise from the LO, which is further magnified by multiplier chains at the transceiver by $20\log_{10}(N)$, where N is the number of multipliers in the up-/downconverter chain³⁴. The phase noise beyond a 1 MHz offset is buried under the digital storage oscilloscope (DSO) amplitude noise

and cannot be traced. However, the phase noise component in the region beyond 1 MHz offset is less than -100 dBc Hz^{-1} , which indicates a remarkably low occurrence of such a huge phase noise component. This makes it insignificant in terms of the communication perspective.

Despite the large chain of frequency multipliers, the phase noise for upconverter 1 at RF is -56 dBc Hz^{-1} at 1 kHz; the corresponding value

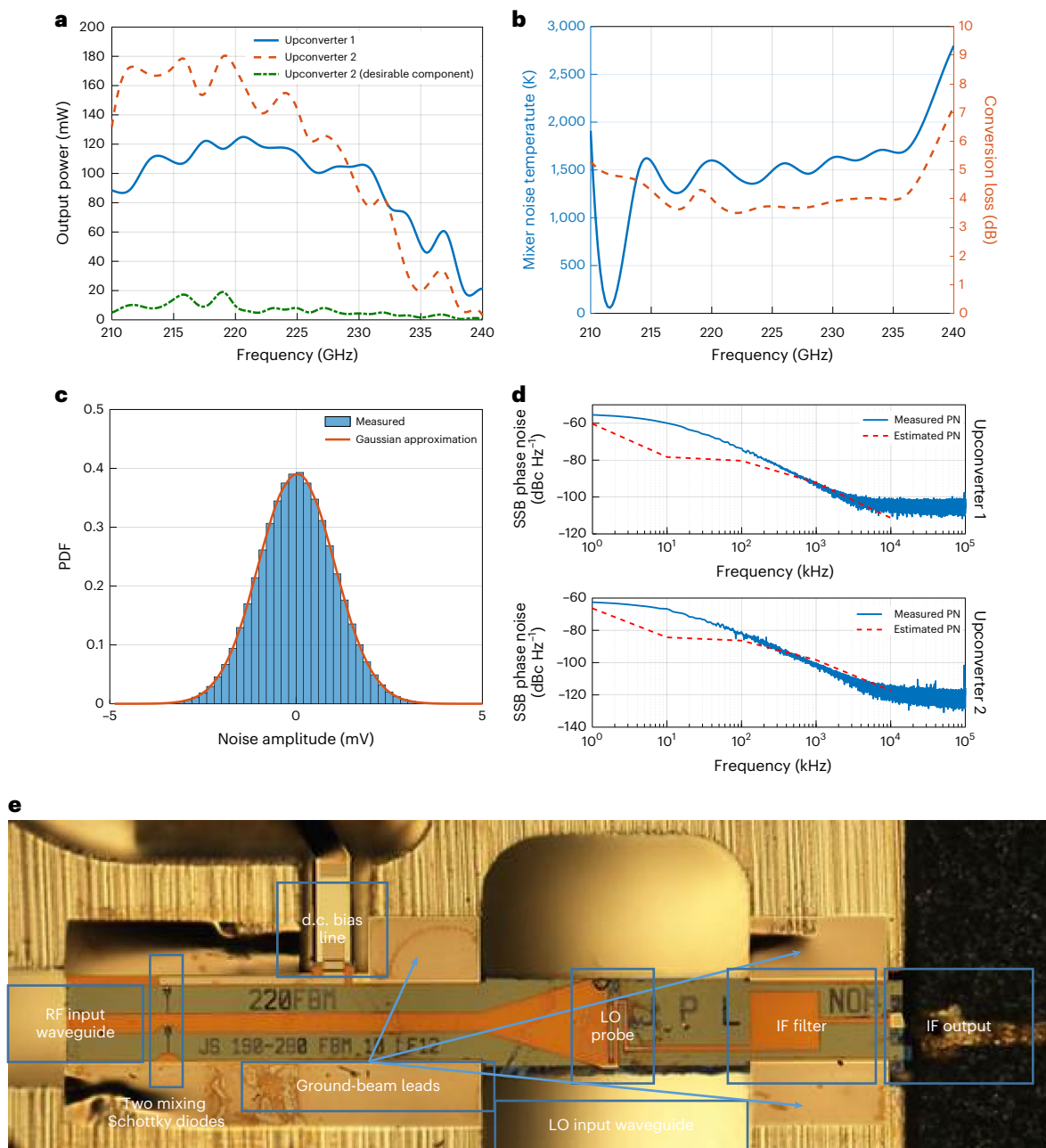


Fig. 2 | Transmitter and receiver performance at 210–240 GHz. **a**, Output power of the two transmitter configurations, namely, upconverter 1 and upconverter 2, and the desirable harmonic of upconverter 2. **b**, Conversion loss and noise temperature of the mixer at the receiver. **c**, Probability density function

(PDF) of the amplitude noise at the receiver, experimental measurement and numerical approximation. **d**, SSB phase noise (PN) for the end-to-end system. **e**, Epitaxial structure of the receiver mixer.

for upconverter 2 is approximately 7 dB lower due to the utilization of a lower multiplier chain at the transmitter. Moreover, the phase noise limits the maximum length of the frame depending on the confinement of most of the energy for phase noise within the given frequency offset, which is 1.7 and 0.8 MHz for upconverter 1 and upconverter 2, respectively (considering an offset point of less than -100 dBc Hz $^{-1}$). Furthermore, upconverter 2 has significant spurs or spurious power in the phase noise spectrum due to the mixer.

Software-defined communication testbed

Although potentially enabling long-range ultrabroadband terahertz links, the developed transceiver architecture requires

tailored communication solutions to ultimately establish a reliable multi-kilometre multi-gigabit-per-second link. More specifically, the nonlinear response of the frequency multipliers needs to be taken into account when defining the waveforms to be transmitted. Due to the aforementioned operational requirements of frequency multipliers, we focus our study in the transmission of phase-modulated signals (M -ary phase-shift keying (M -PSK)).

In the case of LO modulation (upconverter 1), the frequency and phase information at RF corresponds to that of the LO multiplied by the total multiplication factor of the chain (in our setup, a factor of 18). The mathematical demonstration is shown in Methods. Therefore, to ensure that the transmitted signal corresponds to that of a standard

M-PSK, the corresponding phase changes at LO need to be divided by the same factor. When injecting the information through the mixer (upconverter 2), the harmonics at the output of the mixer are processed by the frequency tripler to RF. Interestingly, as derived in Methods, one of the frequency components at RF contains the IF frequency and phase information without any additional multiplication factor. Therefore, at the receiver, adequate filtering is needed to recover this harmonic. In both cases, standard *M*-PSK modulator blocks cannot be utilized. Instead, to accommodate the hardware constraints, we have defined a parametrized tailored modulation function in software (MATLABR2021).

Moreover, beyond modulation/demodulation, there are several additional steps required to reliably transfer information, including over-the-air synchronization, channel estimation and equalization. For this, we have defined a custom frame structure integrated by a synchronization preamble, pilot symbol sequence and actual information to be transmitted (Fig. 3). In our system, we utilize a 20-bit-long predefined pseudo-random sequence for synchronization, which has been shown to have high-autocorrelation and low-crosscorrelation properties. For channel estimation and equalization, we utilize a minimum-mean-square-error-based linear filter equalizer. The filter coefficient vector for post-equalization is obtained by minimizing the difference between the transmitted training symbols and the symbols at the output of the equalizer (Methods). As with the modulator/demodulator blocks, all these functionalities at the transmitter and receiver are implemented in software (Fig. 1e,f).

To interface the software-defined communication physical layer and RF hardware, we leverage a state-of-the-art arbitrary waveform generator (AWG) and DSO with 92 gigasamples per second (Gsp/s) and 160 Gsp/s, respectively (with corresponding baseband bandwidths of 32 and 63 GHz). These are part of the TeraNova testbed³⁵, which has been mainly utilized for very short-range wireless links at frequencies above 1 THz.

End-to-end system

The transmitter and receiver in our system were deployed in two outdoor facilities at 2.03 km between them. Two sets of directional horn-lens antennas with 40 or 55 dB gain per antenna were utilized in different experiments. In addition, a low-noise amplifier (LNA) with 35 dB gain and noise figure of 1 dB is utilized at the receiver to operate on the full dynamic range of the analogue-to-digital converter.

Before data transmission, we characterized the end-to-end frequency response of the system including the transmitter, channel and receiver. In Fig. 4a, we illustrate the measured frequency response for the two transmitter configurations and the two sets of antennas. First, we characterized the source-modulated system (upconverter 1) by simultaneously changing the LO frequency at the transmitter and receiver in fixed steps of 1 GHz, from 210 to 240 GHz. By this process, we were able to separate the impact of mixers and connectors within the transceiver system. However, beyond 235 GHz, the output power of the transmitter dropped significantly. To measure the response of the IF-modulated system (upconverter 2), we kept the LO at the transmitter and receiver constant, as the transmitter IF signal into the mixer is changed in increments of 1 GHz (Fig. 4b). In this case, the power at the IF component without any additional multiplication factor for frequency and phase information is considered. Besides, the transmitter-side mixer frequency response limits the overall usable system bandwidth up to 10 GHz. In both cases, the results demonstrate the ultrabroadband and frequency-selective nature of the end-to-end system. The detailed budget analysis that supports the measured power figures is provided in Methods. Evidently, despite the design specifications, the higher-gain antennas were not able to increase the received power by the expected 30 dB, but by at most 20 dB, even after careful alignment.

To represent the performance of the two different setups of upconverters, the constellation diagram for the received signal (utilizing a 55-dB-gain antenna at the transceiver at a data rate of 1 Gbps) is shown

in Fig. 4c,d for upconverter 1 and upconverter 2, respectively. The recorded error vector magnitude (EVM) for upconverter 1 and upconverter 2 with a 2 Gbps binary phase-shift keying (BPSK)-modulated signal is shown in Fig. 4e. The result affirms the use of higher-order modulation schemes for the upconverter 2 setup. Furthermore, the constellation diagram for higher-order modulation for short distances (<100 m) is shown in Methods.

Finally, we proceeded to the data transmission phase utilizing the proposed frame structure with different modulation strategies and data rates. In Table 1, we summarize our results in terms of bit error rate (BER) for different parameters when utilizing upconverter 1 and upconverter 2. We calculated the BER depending on ten frames, each containing 1,200 bits. All the signals were transmitted at 225 GHz. For the upconverter 1 configuration, the performance in terms of data rate was mainly limited by the multiplication factor (18 times) affecting the modulated LO, which lead to the spreading of the LO bandwidth by the same factor, as well as multiple harmonics. The data rate could not be increased by either reducing the symbol time as it would lead to a larger overlap of the multiple harmonics and therefore lead to waveform distortion or by utilizing higher-modulation orders (for example, quadrature phase-shift keying (QPSK) or 8-PSK) as it would translate to very small phase shifts in the LO (for example, $90^\circ/18 = 5^\circ$), not accurately definable with a state-of-the-art AWG. For the upconverter 2 configuration, the much lower multiplication factor by which the signal is affected (three times) enables the utilization of larger bandwidths as well as higher-modulation orders. In both cases, a higher ratio of energy per bit to noise density (E_b/N_0) is required to maintain the BER, for which we utilized the higher-gain antenna set.

Related work and path forward

Our experimental results demonstrate a terahertz communication link for distances over 1 km, defining a new milestone towards the timely development of sub-terahertz and terahertz communication systems in the context of sixth-generation (6G) networks. Several groundbreaking experimental demonstrations of wireless links at 220 GHz (refs. 36–38), 240 GHz (ref. 39), 300 GHz (refs. 40–46), 625 GHz (ref. 47), 666 GHz (ref. 48) and even 1.05 THz (ref. 49) in Europe, Asia and USA have been conducted in the last decade.

There are mainly two types of testbed: systems aimed at demonstrating high data rates even for short distances (<50 m), and systems aimed at demonstrating the potential use of terahertz communications over long distances (>0.5 km). The reference work in the field is conducted by Fraunhofer Institute³⁹, which simultaneously achieves 64 Gbps over 850 m distance. In another work⁴⁸, a demonstration at 666 GHz has been conducted by Northrop Grumman, which—for the time being—does not outperform the work done by Fraunhofer Institute³⁹, with regard to neither data rate nor distance, but sets the benchmark for the highest carrier frequency. Most recently, Fraunhofer Institute⁴⁶ demonstrated the performance of a wireless link in terms of *Q* factor for 500 m and 1 km distance with data rate of 76 and 44 Gbps, respectively. However, the actual BER for the wireless link was not shown. In any case, data transmission at terahertz frequencies for distances beyond 1 km has not been demonstrated. Moreover, in both the above works^{39,48}, a long communication range was achieved by increasing the antenna gain at the transmitter and receiver (55 dB in both cases). Very high-gain antennas lead to very narrow beams, which require very precise alignment and are affected by ambient vibrations (for example, those resulting from light breeze). In our setup, we are able to demonstrate a multi-kilometre multi-gigabits-per-second link even with 40-dB-gain antennas, because of the much higher output power of the frequency multiplier sources.

Moving forward, there are several steps to improve our hardware and software designs based on the lessons learned in our experiments. On one hand, if increasing the transmission power and ultimately the communication distance is the performance goal, the LO-modulated

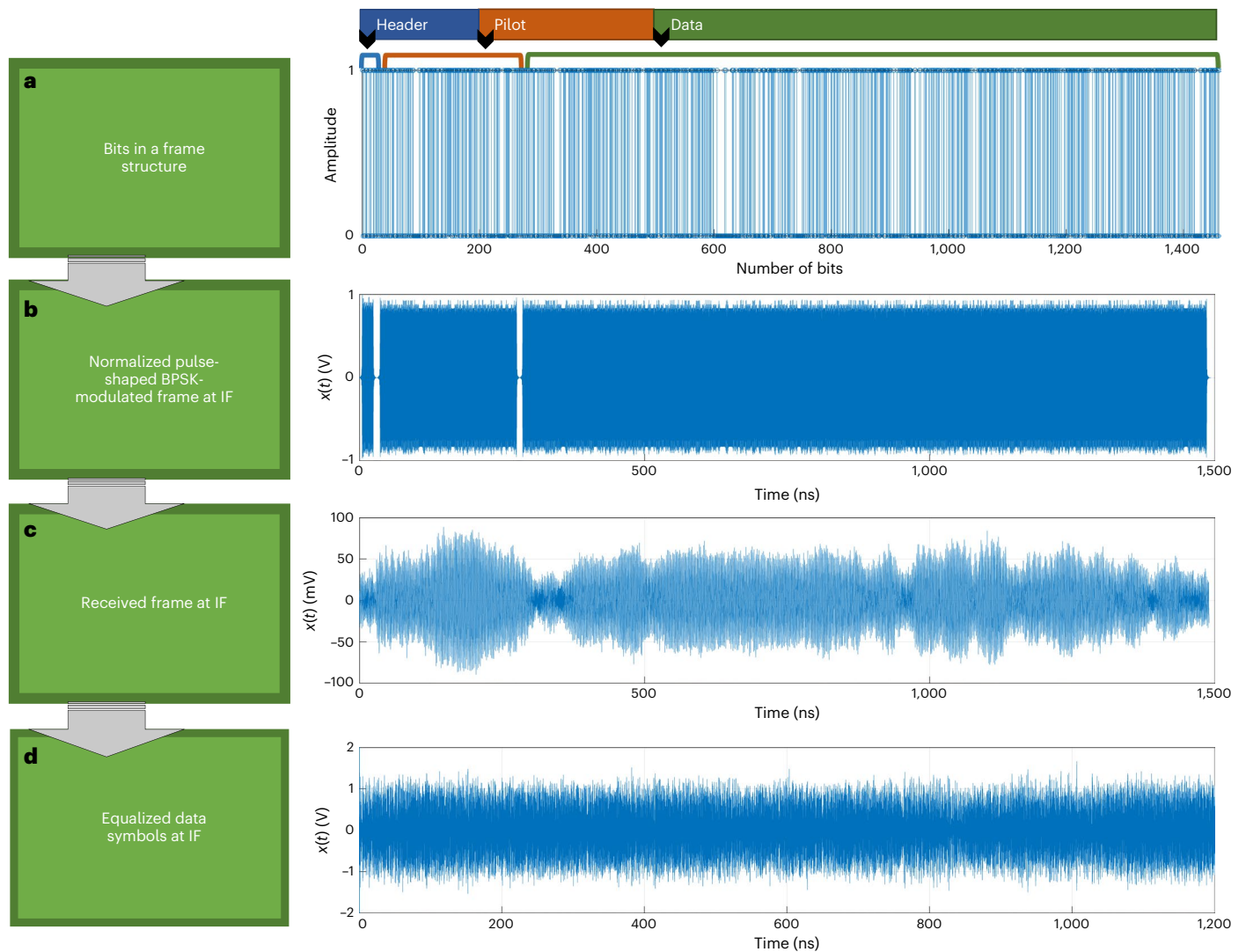


Fig. 3 | Frame definition and its transition from the transmitter to receiver at various stages. a, Binary frame structure, containing the header (20 bits), pilot symbol sequence for channel estimation (240 bits) and data bits (1,200 bits). **b**, A 1 Gbps BPSK-modulated frame at IF, in which pulse shaping has been utilized

to limit the bandwidth of the resulting signal. **c**, Received frame at IF after upconversion, radiation, propagation, detection and downconversion, in which the nonlinear response of the transmitter and receiver hardware is clearly visible. **d**, Data symbols at IF after channel equalization.

system (upconverter 1) benefits from the lack of mixer and its consequent conversion loss. To increase the data rate in this configuration, a multiplier chain with a lower multiplication factor can be utilized, which would enable both higher-modulation orders and larger bandwidths. Nevertheless, the system would still be limited to phase-only modulations, due to the need to ensure that enough power is injected at each multiplier stage. On the other hand, if the driver is increasing the data rate, a mixing block is needed. The injection of the modulated IF at an intermediate stage can partially achieve this; however, ultimately, a mixer at RF would lead to the minimization of harmonics and cleaner waveforms. Other mechanisms to mix in the information into the RF signal could be considered, by leveraging the nature of the frequency multiplier itself, such as through the modulation of power-tripler bias lines. In combination with these approaches, to further increase the distance and data rate, we can leverage multi-source (multi-pixel) systems or arrays. Although non-negligible, 2 Gbps at 2 km could be achieved at lower frequencies (for example, in the 57–71 GHz unlicensed band), where the technology is more mature and propagation conditions are more advantageous, with narrower bandwidths and by utilizing higher-order modulations. Our goal in this work has been to show that with our proposed world-record-setting

terahertz sources, to the best of our knowledge, which were originally conceived for terahertz radar systems and thus required us to rethink how to modulate them, the transmission power might not necessarily be the main challenge anymore, but refined transceiver architectures, innovative signal processing and modulation solutions will be needed²⁵.

Increasing the compactness of the testbed is another required step towards converting this proof-of-concept demonstrator into a practical system with broader impact. First, although the current system is built in a modular way, the final upconverting and downconverting devices can be integrated in a single chip, including the microwave LO sources, all in the sub-30-GHz range. Similarly, in our tests, we utilized a commercial AWG and DSO to generate and process offline the information-carrying ultrabroadband signals. Because we are implementing non-standard modulations, existing commercial *M*-PSK modulation hardware, operating in real time, cannot be utilized. Instead, a field-programmable-gate-array-based system would be needed. Currently, state-of-the-art RF system-on-chip testbeds, integrating a high-performance field-programmable gate array with multiple digital-to-analogue converters and analogue-to-digital converters, are able to support up to 16 channels with over 2 GHz of bandwidth

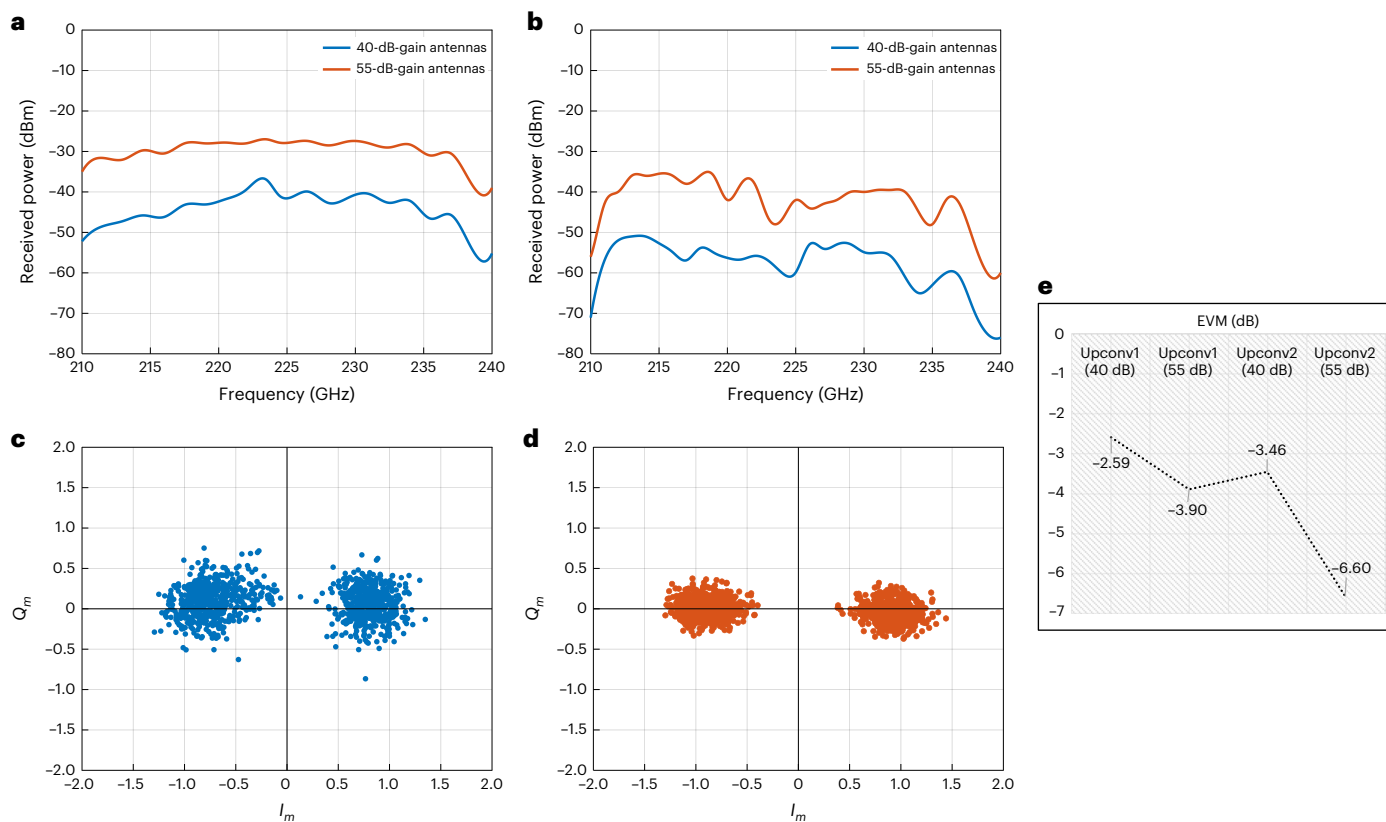


Fig. 4 | Front-end characterization and performance of the 2 km link. **a**, Measured power at the receiver when using upconverter 1 at the transmitter, as a function of the carrier frequency. **b**, Measured power at the receiver when using upconverter 2 at the transmitter, as a function of carrier frequency. **c**, BPSK

constellation obtained for upconverter 1 for a 55 dBi antenna and 1 Gbps signal. **d**, BPSK constellation obtained for upconverter 2 for 55 dBi antenna and 1 Gbps signal. **e**, Recorded EVM for upconverter 1 and upconverter 2 obtained for a 2 Gbps BPSK signal and different antenna gains.

Table 1 | Data transmission using source-modulated (upconverter 1) and IF-modulated (upconverter 2) system

Modulation	Tx/Rx gain (dB)	Bandwidth (GHz)	Bit rate (Gbps)	SNR (dB)	BER
Upconverter 1					
BPSK (×18)	40	2	1	15.6	0*
BPSK (×18)	40	4	2	14.9	0.028
BPSK (×18)	55	2	1	28.0	0*
BPSK (×18)	55	4	2	29.5	0.0035
Upconverter 2					
BPSK	40	2	1	10.0	0*
BPSK	40	4	2	9.0	0.013
BPSK	55	2	1	21.1	0*
BPSK	55	4	2	22.1	0.001
QPSK	40	2	2	10.3	0.003
QPSK	55	2	2	18.5	0*
8-PSK	40	2	3	12.3	0.056
8-PSK	55	2	3	22.0	0.017
16-PSK	40	2	4	10.5	0.1
16-PSK	55	2	4	22.5	0.07
OOK	55	1	0.5	10.2	0*

*0 BER indicates there is no bit error found by averaging over ten frames with 1,200 bits each.

each. We envision the interconnection of custom-programmed radio-frequency systems on chip with multiplexed channels and the RF front ends to be one of the next steps in our research, towards enabling real-time terahertz communication networks, and we are currently working in that direction⁵⁰.

Conclusions

We have reported long-range terahertz communications using compact on-chip high-power terahertz sources and tailored signal processing solutions. Our approach could potentially be used in a range of applications relevant to 6G wireless networks and beyond, including high-capacity wireless backhaul for rural broadband connectivity and quickly deployable emergency network infrastructure following the aftermath of severe weather events where wired (such as optical fibre) infrastructure has been compromised. High-speed wireless links can be used, for example, as the backbone of mesh networks that interconnect user-facing microwave and millimetre-wave access points operating under existing standards (such as IEEE 802.11) with the existing infrastructure of an Internet service provider. This could be done at a fraction of the cost of optical-fibre-based deployment, potentially bridging the digital divide in rural areas.

Further refinement of our architectures could extend communication distances to tens of kilometres. In particular, the main bottleneck in the system is the way in which information-bearing signals are introduced to the high-power frequency multiplier chain. To increase both transmit power and modulation bandwidth, one option would be to directly introduce phase modulation through the control of frequency-tripler bias. This will require, once again, the design of custom signal processing

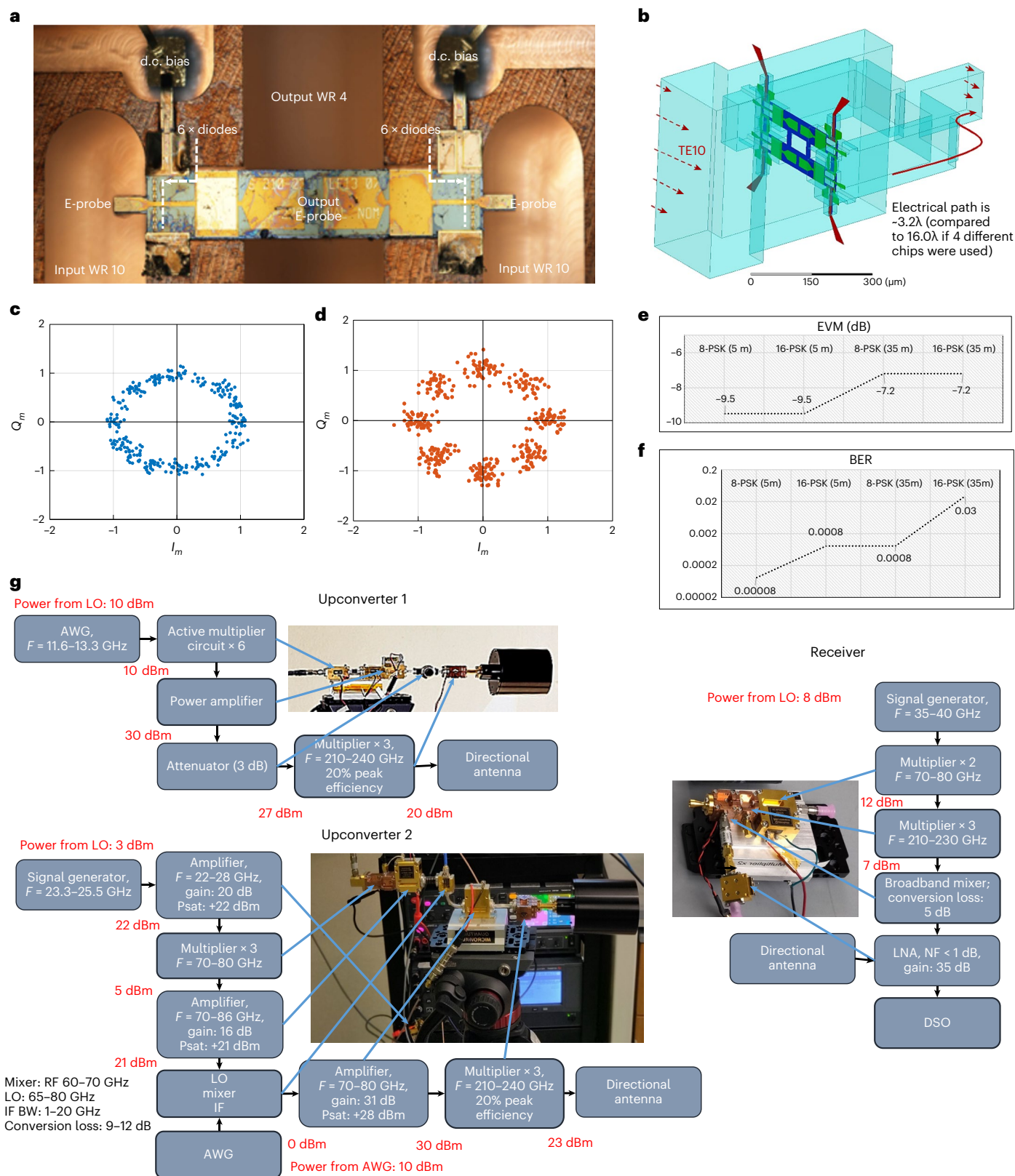


Fig. 5 | JPL's high-power multiplier and detailed front-end system design with capabilities. **a**, Inner configuration of JPL's high-power on-chip power combiner with a 210–240 GHz tripler. **b**, Schematic of on-chip power combining for the hybrid approach. **c**, 16-PSK constellation obtained for upconverter 2 for 40 dBi antenna and 2 Gsps (8 Gbps) signal at 5 m distance. **d**, 8-PSK constellation

obtained for upconverter 2 for 40 dBi antenna and 2 Gsps (6 Gbps) signal at 35 m distance. **e, f**, Recorded EVM (**e**) and BER (**f**) for upconverter 2 obtained for a 2 Gsps signal with 40 dBi antenna. **g**, Full configuration of the transceiver chain with mixers, multipliers and amplifiers with the corresponding powers at different stages.

solutions. Such systems can be developed by having the materials and device community and the communication and signal processing society working in tandem to create jointly optimal solutions. This has not always been the case, even at terahertz frequencies. Due to the inertia in the development of microwave and millimetre-wave devices, existing terahertz transceiver and antenna designs are mainly replicating what has worked at lower frequencies and supporting only conventional communication strategies (for example, traditional modulations and synchronization schemes). Thus, communication solutions might be limited either by the available hardware or might assume capabilities not realizable with current device technologies.

Methods

On-chip power-combining technology for high-power frequency multipliers

To generate the required power at 210–230 GHz frequencies, on-chip power combining, which allows the integration of several multiplier structures in a single chip, is utilized. Traditional power-combining techniques have different difficulties at frequencies beyond 200 GHz. First, devices need to be electrically identical to avoid impedance mismatches; in addition, their precise position in the wafer becomes critical (leading to very low microfabrication tolerances). Furthermore, the manually assembled device's alignment needs to be very accurate to avoid imbalances in the circuit. Also, the performance is degraded when using waveguide-based power combiners (Y junctions and hybrid couplers), since waveguide losses are high at terahertz frequencies. The on-chip power-combining concept overcomes these issues by performing power combining directly 'on chip', and the peak efficiency of 21% is obtained by the process. Since fabrication processes are controlled by the high accuracy of optical lithography and the multiplier structures are physically connected on a single chip, the alignment and symmetry of the circuits are well preserved. This avoids performance loss caused by electrical imbalances when multiple discrete chips are used.

The structural diagram for the on-chip power-combining method is shown in Fig. 5a. Here electrical (E) probes located at the centre of the chip (input waveguide) couple the input signal into multiplier structures. Each multiplier structure features six Schottky diodes that are mounted on single 50 μm GaAs substrate, which is sufficiently thick for good thermal dissipation. In this case, varactor Schottky-diode-based frequency multiplier devices are utilized for fabrication, using the flight-qualified air-bridge planar Schottky diode process successfully used for HIFI²⁶ and MIRO²⁷. Since the complete multiplier structure is fabricated on a single GaAs monolithic microwave integrated circuit, a high level of integration is possible, which allows the use of multiple anodes on the same chip and improves the critical control of matching circuit elements that is crucial in such frequency ranges. In addition, the larger anode size and thicker substrate compared with the traditional design result in an increase in the power-handling capabilities of the circuit. The output signals from the multiplier structures on each side are combined on chip and radiate into the output waveguide.

For upconverter 1 with a transmit signal power of 100 mW, a configuration comprising two multiplier structures is used. However, for upconverter 2 with a transmit signal power of 200 mW, the hybrid approach is adopted. The power is combined from two of those chips mentioned above by using four E probes located at the centre of the chip (input waveguide) and traditional power-combining techniques (Fig. 5b). Here the chip has inherently two outputs that are further combined using a very short Y junction. Moreover, depending on the required power-handling capabilities, a more straightforward configuration consisting only of two multiplier structures can be used for upconverter 1 (only the bottom or top half of the chip; Fig. 5b). Moreover, in Fig. 5g, the detailed description of the transceiver chain with mixers, multipliers and amplifiers with the corresponding powers at different stages is shown to elaborate the performance of upconverter 1, upconverter 2 and receiver.

Phase noise estimation

As described in the main text, to increase reliability and to facilitate the link-layer design, the phase noise is extracted for upconverter 1 as well as upconverter 2 from the IF component (that is, 9 GHz) at the receiver; therefore, it captures the total noise introduced by the upconverting and downconverting chains at the transmitter and receiver, respectively. More specifically, we utilize the DSO to capture 80 megasamples of the received signal when transmitting a non-modulated sinusoidal signal. Leveraging the fast Fourier transform algorithm, we estimate the received signal power spectral density. Then, we compute the relative power leakage over a 1 Hz bandwidth for different frequency offsets with respect to the target carrier frequency. This process leads to the computation of the SSB phase noise in terms of decibels relative to the carrier per Hertz. An average over such 16 experimental readings is conducted to acquire a close estimate.

Software-defined ultrabroadband digital signal processing blocks at the transmitter and receiver

To generate the required signals during transmission and process them during reception and which are tailored to the terahertz device capabilities and terahertz channel behaviour, a back-end digital signal processing engine is utilized. In a nutshell, the user-provided data bits are structured in frames, modulated into symbols and shaped into digital signals to be fed to the front end through the AWG at the transmitter (Fig. 1e). The digitized signals captured by the DSO are synchronized, equalized and demodulated to recover the data bits at the receiver (Fig. 1f).

At the transmitter, the frame is generated by concatenating three parts, namely, header, training sequence and data sequence. The header (20 bits) is a pseudo-random sequence that offers high-autocorrelation and low-crosscorrelation properties and is uniquely suited to detect the beginning of a new frame. The training sequence (up to 200 bits) contains the bits that will be used for channel estimation and equalization purposes. The data sequence contains up to 1,200 user-defined bits. As discussed in the main text, this length is determined after taking the phase noise of the system into consideration. Thereafter, the generated frames are modulated according to M -PSK modulation schemes. Also, for upconverter 2, OOK modulation is considered to observe the performance beyond M -PSK. To obtain the conventional modulated signal at the receiver, the modulation process is modified at the transmitter to cancel out any nonlinear effect produced by the upconverter (discussed below). Thereafter, the raised cosine pulse filter is utilized to restrict the generated signals' spectrum within the transmission bandwidth and—at the receiver—to ease the noise-filtering process. Furthermore, a pre-distortion filter is implemented to compensate for the hardware-deterministic frequency-selective response. In our case, this arises mainly from the frequency-dependent attenuation of the coaxial cables and connectors. Here the inverse of the measured frequency response for each component is used as the frequency-domain coefficient of the pre-equalization filter.

At the receiver, a band-pass filter is utilized to eliminate the out-of-band noise. The detection of the starting point of the captured signal is done by the frame synchronization block. This block correlates the received signal with the same 20-bit-long pseudo-random sequence utilized at the transmitter. A minimum-mean-square-error-based linear filter equalizer is utilized to mitigate the effect of the frequency-selective nature of the channel and path loss. The filter coefficient vector \hat{f} for post-equalization is obtained by minimizing the error between the transmitted training symbols \hat{s} and the symbols of the equalizer output, that is, $R\hat{f}$, where R is the Toeplitz matrix with the received training symbols. The received signal waveform is passed through a correlator-type detector, and the maximum likelihood criterion is utilized to recover the bits. This is an optimal detector provided that the receiver experiences additive Gaussian noise and given by

$$\hat{m} = \underset{1 \leq m \leq M}{\operatorname{argmax}} \left(\int_0^T r(t) x_m(t) dt - \frac{1}{2} \|x_m\|^2 \right), \quad (1)$$

where \hat{m} is the maximum match with a particular symbol and used for bit detection. Furthermore, $m = 1, 2, \dots, M$, M denotes the modulation index and $r(t)$ refers to the received symbol.

LO-modulated and IF-modulated transceiver configurations

Due to the non-conventional upconverter chain needed to achieve high output power, the modulation block in the transmitter software-defined ultrabroadband digital signal processing engine needs to be adapted. For upconverter 1 or LO-modulated system, the phase modulation step or phase shift is obtained by dividing the total angular sweep (that is, 2π) over the multiplication factor utilized by the frequency multiplier chains at the transmitter (that is, 18 in our setup) and the modulation order ($M = 2, 4, \dots$ for BPSK, QPSK...). Then, the phase of the LO input to the multiplier chains is modulated according to the information for each symbol duration. The modified M -PSK constellation is given by

$$I_m = \cos\left(\frac{(m-1)}{18M} 2\pi\right); Q_m = \sin\left(\frac{(m-1)}{18M} 2\pi\right), \quad (2)$$

where $m = 1, \dots, M$ is the index of the information symbol in the transmitter alphabet. Finally, the dividing factor is cancelled by the transmitter multiplier chain; at the output, a conventional M -PSK signal is obtained.

When utilizing this configuration, the achievable BER increases for higher-order modulation because of the very small phase shifts in the injected LO signal. To overcome the problem, the second transmitter configuration, namely, upconverter 2, is defined, which introduces a frequency mixer between two frequency triplers to modulate the information. In this case, one of the harmonics generated at RF has the IF frequency and its phase information without any additional multiplication factor. In particular, the output of the tripler at 210–240 GHz can be derived as

$$\text{RF}_{\text{output}}(t) = ((1 + \cos(\omega_{\text{IF}}t)) \cos(\omega_{\text{LO}}t))^3, \quad (3)$$

where $\omega_{\text{LO}} = 2\pi f_{\text{LO}}$ and $\omega_{\text{IF}} = 2\pi f_{\text{IF}}$, with $f_{\text{LO}} \in [70\text{--}80]$ GHz and $f_{\text{IF}} \in [0\text{--}10]$ GHz. In equation (3), ‘1’ is utilized to represent any LO leakage from the mixer. By operating on this equation, the output-signal frequency components are given by

$$\begin{aligned} \text{RF}_{\text{output}}(t) = & \frac{1}{32} (15 \cos(\omega_{\text{IF}} - 3\omega_{\text{LO}})t + 6 \cos(2\omega_{\text{IF}} - 3\omega_{\text{LO}})t \\ & + \cos(3\omega_{\text{IF}} - 3\omega_{\text{LO}})t + 45 \cos(\omega_{\text{IF}} - \omega_{\text{LO}})t \\ & + 18 \cos(2\omega_{\text{IF}} - \omega_{\text{LO}})t + 3 \cos(3\omega_{\text{IF}} - \omega_{\text{LO}})t \\ & + 45 \cos(\omega_{\text{IF}} + \omega_{\text{LO}})t + 18 \cos(2\omega_{\text{IF}} + \omega_{\text{LO}})t \\ & + 3 \cos(3\omega_{\text{IF}} + \omega_{\text{LO}})t + 15 \cos(\omega_{\text{IF}} + 3\omega_{\text{LO}})t \\ & + 6 \cos(2\omega_{\text{IF}} + 3\omega_{\text{LO}})t + \cos(3\omega_{\text{IF}} + 3\omega_{\text{LO}})t \\ & + 60 \cos(\omega_{\text{LO}})t + 20 \cos(3\omega_{\text{LO}})t) \end{aligned} \quad (4)$$

The lower-frequency terms (that is, signals at ω_{LO}) are filtered by the tripler and antenna frequency response. The terms of interest are those at $3\omega_{\text{LO}}$, given by

$$\begin{aligned} \text{RF}_{\text{output}}(t) = & \frac{1}{32} (15 \cos(\omega_{\text{IF}} \pm 3\omega_{\text{LO}})t + 6 \cos(2\omega_{\text{IF}} \pm 3\omega_{\text{LO}})t \\ & + \cos(3\omega_{\text{IF}} \pm 3\omega_{\text{LO}})t + 20 \cos(3\omega_{\text{LO}})t). \end{aligned} \quad (5)$$

Utilizing a suitable filter (in our system, a digital filter), the modulated signal without any additional multiplication factor can be

extracted, which enables us to directly use a standard M -PSK modulation at IF:

$$\text{RF}_{\text{output}}(t) = \frac{1}{32} (15 \cos(\omega_{\text{IF}} \pm 3\omega_{\text{LO}})t). \quad (6)$$

However, due to the $\times 3$ multiplier response, the power at $f_{\text{IF}} + -3f_{\text{LO}}$ component is comparatively lower than the $3f_{\text{IF}} + -3f_{\text{LO}}$ component. Still, by considering the $f_{\text{IF}} + -3f_{\text{LO}}$ component, we can modulate the signal with higher-order M -PSK, as we do not have to compensate for the multiplication factor. Therefore, the modulated symbol is given by

$$I_m = \cos\left(\frac{(m-1)}{M} 2\pi\right); Q_m = \sin\left(\frac{(m-1)}{M} 2\pi\right). \quad (7)$$

The performance comparison between two upconversion systems for a 2 km link is explained by the constellation plots in the end-to-end wireless communication system (main text). In this section, the capability of upconverter 2 is shown by utilizing the higher-order modulation for short-distance links. The constellation diagram of 16-PSK and 8-PSK modulations (with symbol rate of 2 Gsps) are shown for 5-m- and 35-m-long wireless links (Fig. 5c,d, respectively). Here 40-dBi-gain antennas are utilized to create the link. In Fig. 5e, the obtained EVM is illustrated for the setup, which is significantly low to support different modulation schemes. Further, in Fig. 5f, the performance of upconverter 2 in terms of BER, respectively, for high-order modulation for distances up to 35 m is shown.

Data availability

The data corresponding to the raw received signals at the IF for the different configurations shown in Table 1 are available from the corresponding author upon request. Because the experiments were conducted at the US Air Force Research Laboratory (AFRL) Information Directorate’s Newport Research facilities, as indicated in the manuscript, a Cooperative Research and Development Agreement or memorandum of understanding is needed between the requester’s organization, authors’ organization and/or sponsoring organization, which in this case is the US Air Force Research Laboratory AFRL. To obtain such an agreement, please contact the corresponding author, who will guide the requester through the necessary steps. Source data are provided with this paper.

Code availability

The codes utilized for the generation of the signals at the transmitter and for the processing of the measured signals at the receiver. Because the experiments were conducted at the US AFRL Information Directorate’s Newport Research facilities, as indicated in the manuscript, a Cooperative Research and Development Agreement or memorandum of understanding is needed between the requester’s organization, authors’ organization and/or sponsoring organization, which in this case is the US AFRL. To obtain such an agreement, please contact the corresponding author, who will guide the requester through the necessary steps.

References

1. US Federal Communications Commission. *Winning Bidders Announced for Auction of 28 GHz Upper Microwave Flexible Use Service Licenses (Auction 101)* (accessed 10 December 2019); <https://docs.fcc.gov/public/attachments/FCC-18-109A1.pdf>
2. US Federal Communications Commission. *Auction 103: Spectrum Frontiers—Upper 37 GHz, 39 GHz, and 47 GHz* (accessed 10 December 2019); <https://www.fcc.gov/auction/103>
3. US Federal Communications Commission. *FCC Opens Spectrum Horizons for New Services & Technologies*

- (accessed 10 December 2019); <https://www.fcc.gov/document/fcc-opens-spectrum-horizons-new-services-technologies-0>
4. Akyildiz, I. F., Han, C., Hu, Z., Nie, S. & Jornet, J. M. Terahertz band communication: an old problem revisited and research directions for the next decade. *IEEE Trans. Commun.* **70**, 4250–4285 (2022).
 5. Rappaport, T. S. et al. Wireless communications and applications above 100 GHz: opportunities and challenges for 6G and beyond. *IEEE Access* **7**, 78729–78757 (2019).
 6. Elayan, H., Amin, O., Shihada, B., Shubair, R. M. & Alouini, M.-S. Terahertz band: the last piece of RF spectrum puzzle for communication systems. *IEEE Open J. Commun. Soc.* **1**, 1–32 (2019).
 7. Abadal, S., Solé-Pareta, J., Alarcón, E. & Cabellos-Aparicio, A. Nanoscale wireless communications as enablers of massive manycore architectures. in *Nanoscale Networking and Communications Handbook* 437 (CRC Press, 2019).
 8. Akyildiz, I. F. & Kak, A. The internet of space things/cubesats. *IEEE Netw.* **33**, 212–218 (2019).
 9. Jornet, J. M. & Akyildiz, I. F. Channel modeling and capacity analysis for electromagnetic wireless nanonetworks in the terahertz band. *IEEE Trans. Wireless Commun.* **10**, 3211–3221 (2011).
 10. Federici, J. F., Ma, J. & Moeller, L. Review of weather impact on outdoor terahertz wireless communication links. *Nano Commun. Netw.* **10**, 13–26 (2016).
 11. Sengupta, K., Nagatsuma, T. & Mittelman, D. M. Terahertz integrated electronic and hybrid electronic–photonic systems. *Nat. Electron.* **1**, 622–635 (2018).
 12. Nikpaik, A., Shirazi, A. H. M., Nabavi, A., Mirabbasi, S. & Shekhar, S. A 219-to-231 GHz frequency-multiplier-based VCO with 3% peak d.c.-to-RF efficiency in 65-nm CMOS. *IEEE J. Solid-State Circuits* **53**, 389–403 (2018).
 13. Aghasi, H., Cathelin, A. & Afshari, E. A 0.92-THz SiGe power radiator based on a nonlinear theory for harmonic generation. *IEEE J. Solid-State Circuits* **52**, 406–422 (2017).
 14. Deal, W. R. et al. A 660 GHz up-converter for THz communications. In *2017 IEEE Compound Semiconductor Integrated Circuit Symposium (CSICS)* 1–4 (IEEE, 2017).
 15. Leuther, A. et al. 20 nm metamorphic HEMT technology for terahertz monolithic integrated circuits. In *2014 9th European Microwave Integrated Circuit Conference* 84–87 (IEEE, 2014).
 16. Urteaga, M., Griffith, Z., Seo, M., Hacker, J. & Rodwell, M. J. InP HBT technologies for THz integrated circuits. *Proc. IEEE* **105**, 1051–1067 (2017).
 17. Mehdi, I., Siles, J. V., Lee, C. & Schlecht, E. THz diode technology: status, prospects, and applications. *Proc. IEEE* **105**, 990–1007 (2017).
 18. Song, H.-J. et al. Uni-travelling-carrier photodiode module generating 300 GHz power greater than 1 mW. *IEEE Microw. Wireless Compon. Lett.* **22**, 363–365 (2012).
 19. Huang, S.-W. et al. Globally stable microresonator Turing pattern formation for coherent high-power THz radiation on-chip. *Phys. Rev. X* **7**, 041002 (2017).
 20. Nagatsuma, T., Ducournau, G. & Renaud, C. C. Advances in terahertz communications accelerated by photonics. *Nat. Photon.* **10**, 371–379 (2016).
 21. Lu, Q., Wu, D., Sengupta, S., Slivken, S. & Razeghi, M. Room temperature continuous wave, monolithic tunable THz sources based on highly efficient mid-infrared quantum cascade lasers. *Sci. Rep.* **6**, 23595 (2016).
 22. Han, C., Akyildiz, I. F. & Gerstacker, W. H. Timing acquisition and error analysis for pulse-based terahertz band wireless systems. *IEEE Trans. Vehicular Technol.* **66**, 10102–10113 (2017).
 23. Peng, B. & Kürner, T. Three-dimensional angle of arrival estimation in dynamic indoor terahertz channels using a forward–backward algorithm. *IEEE Trans. Vehicular Technol.* **66**, 3798–3811 (2016).
 24. Bodet, D., Sen, P., Hossain, Z., Thawdar, N. & Jornet, J. M. Hierarchical bandwidth modulations for ultra-broadband communications in the terahertz band. *IEEE Trans. Wireless Commun.* <https://doi.org/10.1109/TWC.2022.3207966> (2022).
 25. Sen, P., Ariyaratna, V. & Jornet, J. M. An optimized *M*-ary amplitude phase shift keying scheme for ultrabroadband terahertz communication. In *2022 IEEE 19th Annual Consumer Communications & Networking Conference (CCNC)* 661–666 (IEEE, 2022).
 26. De Graauw, T. et al. The Herschel-heterodyne instrument for the far-infrared (HIFI). *EAS Publ. Ser.* **34**, 3–20 (2009).
 27. Gulkis, S. et al. MIRO: microwave instrument for Rosetta Orbiter. *Space Sci. Rev.* **128**, 561–597 (2007).
 28. Perez, J. V. S. et al. On-chip power-combining for high-power schottky diode based frequency multipliers. US patent 9,143,084 (2015).
 29. Siles, J. V. et al. A new generation of room-temperature frequency-multiplied sources with up to 10× higher output power in the 160-GHz–1.6-THz range. *IEEE Trans. THz Sci. Technol.* **8**, 596–604 (2018).
 30. Schlecht, E. et al. Schottky diode based 1.2 THz receivers operating at room-temperature and below for planetary atmospheric sounding. *IEEE Trans. THz Sci. Technol.* **4**, 661–669 (2014).
 31. Schlicht, E., Gill, J., Siegel, P., Oswald, J. & Mehdi, I. Novel designs for submillimeter subharmonic and fundamental Schottky mixers (2003).
 32. Mavric, U., Chase, B. & Fermilab. Residual phase noise measurements of the input section in a receiver (2007); <https://www.osti.gov/biblio/920720>
 33. Montress, G. K., Parker, T. E. & Loboda, M. J. Residual phase noise measurements of VHF, UHF, and microwave components. *IEEE Trans. Ultrason., Ferroelectr., Freq. Control* **41**, 664–679 (1994).
 34. Hausman, H. The effect of high stability reference oscillators on system phase noise. *Microw. J.* **48**, 140–147 (2005).
 35. Sen, P. & Jornet, J. M. Experimental demonstration of ultra-broadband wireless communications at true terahertz frequencies. In *2019 IEEE 20th International Workshop on Signal Processing Advances in Wireless Communications (SPAWC)* 1–5 (IEEE, 2019).
 36. Kallfass, I. et al. All active MMIC-based wireless communication at 220 GHz. *IEEE Trans. THz Sci. Technol.* **1**, 477–487 (2011).
 37. Kallfass, I. et al. Broadband active integrated circuits for terahertz communication. In *European Wireless 2012; 18th European Wireless Conference 2012* 1–5 (VDE, 2012).
 38. Koenig, S. et al. Wireless sub-THz communication system with high data rate. *Nat. Photon.* **7**, 977–981 (2013).
 39. Kallfass, I. et al. 64 Gbit/s transmission over 850 m fixed wireless link at 240 GHz carrier frequency. *J. Infrared Milli. Terahz. Waves* **36**, 221–233 (2015).
 40. Jastrow, C. et al. 300 GHz transmission system. *Electron. Lett.* **44**, 213–214 (2008).
 41. Jastrow, C. et al. Wireless digital data transmission at 300 GHz. *Electron. Lett.* **46**, 661–663 (2010).
 42. Song, H.-J. et al. Terahertz wireless communication link at 300 GHz. In *2010 IEEE International Topical Meeting on Microwave Photonics* 42–45 (IEEE, 2010).
 43. Song, H.-J. et al. 24 Gbit/s data transmission in 300 GHz band for future terahertz communications. *Electron. Lett.* **48**, 953–954 (2012).

44. Ma, J., Karl, N. J., Bretin, S., Ducournau, G. & Mittleman, D. M. Frequency-division multiplexer and demultiplexer for terahertz wireless links. *Nat. Commun.* **8**, 729 (2017).
45. Belem-Goncalves, C. et al. 300 GHz quadrature phase shift keying and QAM16 56 Gbps wireless data links using silicon photonics photodiodes. *Electron. Lett.* **55**, 808–810 (2019).
46. Castro, C., Elschner, R., Merkle, T., Schubert, C. & Freund, R. Long-range high-speed THz-wireless transmission in the 300 GHz band. In *2020 Third International Workshop on Mobile Terahertz Systems (IWMTS) 1–4* (IEEE, 2020).
47. Moeller, L., Federici, J. & Su, K. 2.5 Gbit/s duobinary signalling with narrow bandwidth 0.625 terahertz source. *Electron. Lett.* **47**, 856–858 (2011).
48. Deal, W. R. et al. A 666 GHz demonstration crosslink with 9.5 Gbps data rate. In *2017 IEEE MTT-S International Microwave Symposium (IMS) 233–235* (IEEE, 2017).
49. Sen, P. et al. The TeraNova platform: an integrated testbed for ultra-broadband wireless communications at true terahertz frequencies. *Computer Netw.* **179**, 107370 (2020).
50. Abdellatif, H., Ariyaratna, V., Petrushkevich, S., Madanayake, A. & Jornet, J. M. Real-time ultra-broadband software-defined radio platform for terahertz communications. In *IEEE INFOCOM 2022—IEEE Conference on Computer Communications Workshops (INFOCOM WKSHPS) 1–2* (IEEE, 2022).

Acknowledgements

P.S. and J.M.J. were supported in part by the US Air Force Research Laboratory grant FA8750-20-1-0200 and the US National Science Foundation grant CNS-2011411. J.V.S. was supported by the US Air Force Research Laboratory (AFRL) and JPL Advance Concept Funds program. We would like to acknowledge K. Gross (US Air Force) and AFRL interns, C. Bosso, J. Hall and C. Slezak, for help during data collection of the project. We would like to thank J. Heinig, AFRL Newport Research Facilities manager and the PAR Government Systems Corporation team led by J. Wille and D. Overrocker who helped us with the test setup, coordination and antenna mount fabrication during our experiment at Newport Research Facilities. Any opinions, findings, and conclusions or recommendations expressed

in this material are those of the author(s) and do not necessarily reflect the views of AFRL. Approved for Public Release; Distribution Unlimited: AFRL-2022-5484.

Author contributions

All the authors contributed to the problem definition, conceived and designed the experiments, analysed the data, contributed materials and wrote the paper.

Competing interests

The authors declare no competing interests.

Additional information

Supplementary information The online version contains supplementary material available at <https://doi.org/10.1038/s41928-022-00897-6>.

Correspondence and requests for materials should be addressed to Priyangshu Sen, Jose V. Siles, Ngwe Thawdar or Josep M. Jornet.

Peer review information *Nature Electronics* thanks Nicoleta Cristina Gaitan and the other, anonymous, reviewer(s) for their contribution to the peer review of this work.

Reprints and permissions information is available at www.nature.com/reprints.

Publisher's note Springer Nature remains neutral with regard to jurisdictional claims in published maps and institutional affiliations.

Springer Nature or its licensor (e.g. a society or other partner) holds exclusive rights to this article under a publishing agreement with the author(s) or other rightsholder(s); author self-archiving of the accepted manuscript version of this article is solely governed by the terms of such publishing agreement and applicable law.

© The Author(s), under exclusive licence to Springer Nature Limited 2022